# Efficient target acceleration using underwater electrical explosion of wire array SCI F

View Online  Export Citation  CrossMark

D. Maler,[a] ID A. Rososhek, ID S. Efimov, A. Virozub, ID and Ya. E. Krasik ID

## AFFILIATIONS

Physics Department, Technion, Haifa 32000, Israel

[a]Author to whom correspondence should be addressed: daniel.maler@campus.technion.ac.il

## ABSTRACT

The results of experimental studies together with numerical and analytical modeling showed that the acceleration of a target by employing the shock compression and water flow generated by the underwater electrical explosion of a wire array can be considered an efficient (up to ~20%) approach. In experiments, a pulse generator with stored energy of ~6.5 kJ, current amplitude of ~380 kA, and rise time of ~1.2 $\mu$s was used for underwater electrical explosion of a copper wire planar array. Streak shadow imaging and photonic Doppler velocimetry were applied to study the time-resolved velocity of the shock in water and an aluminum target in air, respectively. The targets, having different thicknesses and designs, were positioned at variable distances from the array. Experimental results showed that the target velocity evolution is characterized by an ns-timescale rise time peak with a subsequent decrease, which transfers to a $\mu$s-timescale increase up to its saturated value. Target velocities of up to 1360 m/s were measured. The experimental, numerical, and analytical modeling results showed that a temporally unmovable barrier, located between the exploding array and the target, allows one to increase the pressure in that location, which leads to higher shock velocity in the target.

## I. INTRODUCTION

Studies of the equation of states (EOS) of different materials at extreme pressures and densities are of great importance for various fields of research. In planetary astronomy, it is crucial to determine the properties of matter in extreme environments, such as giant planets and brown dwarfs.[1] Additionally, the study of the properties of wall material, together with the confirmation of the transport parameters of the cone guide material,[2] promote technological developments for achieving nuclear fusion. A commonly used method to achieve extreme conditions is shock compression.[3] Shock waves realized inside the material of interest are produced by either a focused powerful pulse laser or the interaction of the material with a high-velocity flyer plate. Because of the high energy density deposition that leads to the formation of hot, dense ablation plasma, the laser approach allows the generation of shock pressures reaching $2 \times 10^{12}$ Pa,[4] but only in a small sample with typical dimensions of several tens to hundreds of micrometers. In the case of a flyer plate, its acceleration to high velocities is achieved by applying chemical explosions, gas guns, or magnetic field gradients. When gas guns are applied, flyer plate velocities up to 10 km/s were obtained by a planar shock with pressure up to $10^{11}$ Pa.[5]

The approach based on flyer plate acceleration using magnetic field gradients requires high-current ns-timescale pulse generators. The application of the high-current Z-accelerator,[6] with stored energy up to 22 MJ, allows the acceleration of an aluminum (Al) flyer plate with a weight of ~0.86 g to 34 km/s (kinetic energy ~0.5 MJ) and a quasi-isentropic pressure buildup of up to $5 \times 10^{11}$ Pa.[7] These methods of achieving high pressures and densities in matter via shock compression require large and rather expensive facilities.

In earlier research,[8,9] it was shown that the efficiency of the stored energy transfer to the generated water flow by underwater electrical explosions of a wire can be estimated to be in the range of 15%–24%. Laser and optical time- and space-resolved diagnostics accompanied by hydrodynamic (HD) simulations were applied to estimate the energy transfer to water flow within a few $\mu$s using an ns-timescale underwater electrical explosion of a single wire.[8] In Ref. 9, a time-of-flight method was used to determine the velocity of different Al targets, varying in thickness, placed in water at an 8 mm distance from the wire array, where explosion occurs in the $\mu$s timescale. Based on the experimental results obtained, as well as those of hydrodynamic simulations, it was estimated that the efficiency of the energy transfer to water flow is as high as 24%. In this

study, the energy transferred to the generated water flow was calculated until ~10 $\mu$s with respect to the beginning of the discharge current.

Recently, it was shown[10] that the discharge channel's expansion evolves for a longer period, suggesting that the estimated total efficiency of the energy transfer might be underestimated. It was also shown that, in the case of a planar wire array, an almost simultaneous electrical explosion of wires results in the generation of a uniform planar shock, which retains its symmetry up to a 20 mm distance from the array.[11] Additionally, the results of hydrodynamic numerical simulations and analytical modeling[12] showed that this method can be used for quasi-isentropic target compression up to $2 \times 10^{11}$ Pa with a relatively small energy input into the wires.

In this paper, we present the first results of utilizing a strong shock, generated by the $\mu$s-timescale underwater electrical explosion of a wire array, to accelerate an Al target efficiently. This approach, scaled to the case where greater energy is deposited into the wire array than in the present research, can be considered an attractive method for accelerating flyer plates, as used in the study of material properties. The acceleration of an Al target by generated shocks and water flow was studied with and without thin Perspex plates located between the target and the array positioned 0.5–4 mm apart. Photonic Doppler velocimetry (PDV) was used to measure the velocity of the target. Streak shadow imaging was applied to study the propagation of the shock in water together with shock and target propagation in air. The data obtained for shock propagation in the water together with the electrical power deposited into the exploding array were used to run a one-dimensional hydrodynamic simulation (1DHD)[13] coupled with the EOS for the water, air, plastic, and wire material.[14] This simulation assumed both axial and azimuthal symmetries, typical to cylindrical and spherical geometries. It was shown in earlier research[11] that the diverging planar shock conserves its planarity approximately up to a distance of half the array's width. In the present research, the array's half-width was 2 cm and the maximal array–target distance

was 4 mm. In simulations, the artificially enlarged cylindrical geometry of the simulated volume was used. That is, we considered the converging cylindrical shock as planar at small distances from the array. In the present simulations, it was found that the conditions of planarity along 10 mm of the target width are satisfied, given a cylinder with a radius of 10 cm.

## II. EXPERIMENTAL SETUP AND DIAGNOSTICS

The experimental setup and diagnostics are shown in Fig. 1. A high-current generator,[15] based on four Maxwell-type high-voltage, low-inductance capacitors (total capacitance of 10.6 $\mu$F), and four multi-gap gas switches,[16] was used for the underwater electrical explosion of the planar Cu wire array. These switches were triggered by one trigger pulse of 70 kV and a rise time of 10 ns produced by the Maxwell 40230 trigger amplifier pulse generator. The triggering pulse was delivered by a high-voltage insulated wire through holes made in the middle row balls, thus providing, via capacitance coupling, non-complete discharges between these balls and both high-voltage and grounded electrodes. These discharges initiate, almost simultaneously, the main discharge of all four switches. At charging voltage of 27 kV and 35 kV (for gaps of 6.5 mm and 8 mm between the electrodes, the calculated electric field at the electrode surface does not exceed 28 kV/cm), we estimate the time jitter to be around ±20 ns using simulated and experimentally measured discharge current waveforms.

In the experiments, the generator charged to either 27 kV (stored energy of ~3.8 kJ) or 35 kV (stored energy of ~6.5 kJ) delivers to the short-circuit load pulses with a quarter-period of ~1.2 $\mu$s and amplitudes ~270 kA and ~380 kA, respectively. The waveforms of the discharge current ($I$) and voltage ($V$) were measured using a self-integrated Rogowski coil (measurement error of $\pm 5\%$) and a Tektronix P6015A voltage divider (measurement error of $\pm 3\%$). The total inductance of the discharge circuit and inductance of the load, measured in a short-circuit experiment, was calculated to be
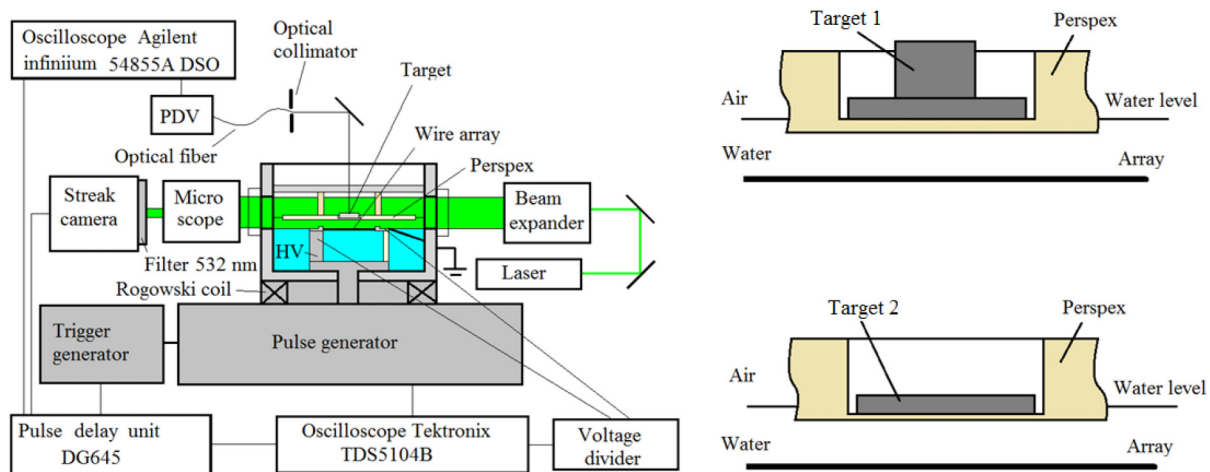


**FIG. 1.** Experimental setup and diagnostics.

~65 nH and ~20 nH, respectively. In this experiment, a planar thick foil with the same length and width as the wire array was used; thus, no significant heating of the load has occurred. Also, in this short-circuit experiment, the total resistance of the discharge circuit was calculated to be ~14 mΩ. The inductive voltage $L\frac{dI}{dt}$, where $L \sim 20$ nH is the planar wire array inductance, was subtracted from the measured value of $V$ to obtain the resistive component of the voltage drop $V_{res}$. The array, consisting of 40 Cu wires having a length of 45 mm, with a ~1 mm distance between neighboring wires (total cross-sectional area of the array is $\sim 18$ cm$^2$), was placed between the cathode and anode electrodes inside an experimental chamber filled with de-ionized water. The distance between the high-voltage side of the array and the chamber wall was ~15 mm. The chamber was made of a 100 mm inner diameter aluminum tube with wall thickness of 40 mm and height of 130 mm. The chamber has two 20 mm diameter windows placed at 180° with respect to each other. The windows were hermitically sealed by 15 mm Perspex plates, which are protected from both sides by 5 mm-thick resin layers with a 10 mm diameter inner hole. To obtain an almost critically damped discharge, such that most of the energy stored in the capacitors is transferred to the exploding array, the wire diameter was adjusted. That is, for 27 kV and 35 kV charging voltages, wires with diameters of 100 μm and 130 μm, respectively, were used. The waveforms of the discharge current, resistive voltage, deposited power, and energy for array explosions at a 27 kV and 35 kV charging voltage of the generator are presented in Fig. 2. One can see that both discharges can be characterized as critically damped with ~80% (~3 kJ for 27 kV) of the stored energy deposited into the array during ~0.8 μs. During these explosions, the resistivity of a single wire increases drastically, reaching ~12 Ω and ~7 Ω for 27 kV and 35 kV, respectively, and the energy density deposition reaches several eV/atom. The latter
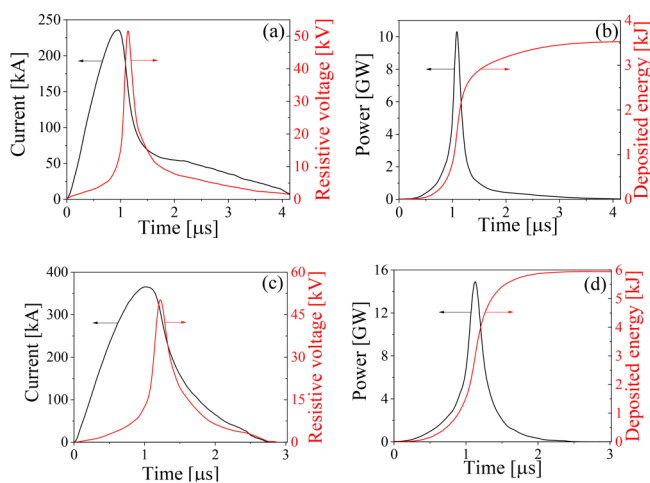
indicates that the wire's explosion results in the formation of low conductivity plasma channels.

The majority of the experiments were conducted using a cylindrical Al target (see Fig. 1, target 1) having a 1 mm-thick bottom part with a diameter of 12 mm and a 2 mm-thick upper part with a diameter of 5 mm with a total weight of 0.4 g. The target was placed on top of a Perspex plate, the thickness of which was varied in the range 0.2 mm–2 mm (see Fig. 1). The Perspex plate, with the target placed upon it, was immersed in water at a ~1 mm depth. The distance between the array and the plate was measured with an accuracy of ±35 μm using a preliminarily calibrated streak camera and was varied in the range of 0.5 mm–4 mm. In several experiments, we tested the acceleration of Al targets (see Fig. 1, target 2) having a thickness of 0.5 mm and 0.02 mm and a diameter of 12 mm. The time at which the shock entered and exited the target was estimated using streak images with an accuracy of ±40 ns due to the smearing of the shock front over ±5 pixels.

A diode-pumped continuous wave (CW) single-mode laser (~1.5 W, $\lambda_g = 532$ nm) was used to backlight the exploding wires, target, and the shock generated in water and air. The shadow images of shocks in water and air together with the target trajectory were obtained using a streak Optronis Optoscope SC-10 camera, which was synchronized with the high-current generator operation. The streak slit, having a width of 100 μm, was positioned in the perpendicular direction with respect to the target, and it was adjusted to view the center of the target along its height. Velocity calculation from the streak images gives an estimated error of ±100 m/s.

The target velocity was extracted using the PDV method[17,18] (see Fig. 3). A single-mode main laser beam produced by the CW laser (~250 mW, $\lambda_m = 1550.12$ nm) was directed using optical fibers toward the circulator having fixed polarization, and, using mirrors M1 and M2, the beam was guided toward the Al target. Before the experiment, the reflected light from the target, located in the experimental chamber closed by a glass window, was adjusted to obtain a reflected power of ~15–50 μW. The reference laser was set to ~500 μW with a wavelength of $\lambda_r = 1550.132$ nm. The interfered light of the reflected and reference laser beams generated a beat signal with a frequency of $f_b = 1.5 \pm 0.1$ GHz. The parasitic crosstalk between Port 1 and Port 3 of the circulator was ~1 μW. The time-base of the PDV measurement was set to 5 μs/div, which allows registration of the time evolution of the interfered signal



**FIG. 2.** Waveforms of the discharge current and resistive voltage [(a) and (c)] and calculated deposited power and energy [(b) and (d)], for 27 kV [(a) and(b)] and 35 kV [(c) and (d)] charging voltage of the pulse generator.
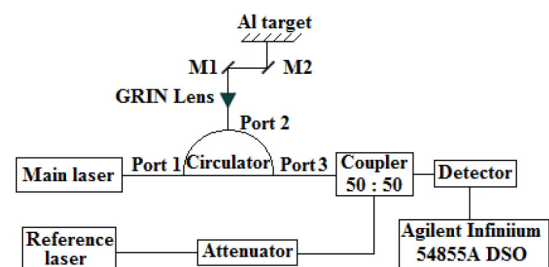


**FIG. 3.** Photonic Doppler velocimetry scheme used in the experiment.

during 50 $\mu$s. The recorded PDV waveform was acquired using an Agilent Infiniium 54855A DSO digitizing oscilloscope (bandwidth of 6 GHz, sampling rate of 20 Gs/s). The PDV analysis frequency resolution is 30 MHz, which gives an estimated error of the extracted target velocity $\pm 25$ m/s. A Stanford DG645 time delay generator was used for synchronization of the operation of the high-current generator, streak camera, and PDV signal registration.

## III. EXPERIMENTAL RESULTS

The first experiments were conducted without target acceleration. In Fig. 4(a), the streak shadow image of the shock in water and air accompanied by water flow is shown for the 35 kV charging voltage of the generator. Let us note that the microscope, seen in Fig. 1, flips all the streak images, so that the generation of the shock appears in the upper part of the image and it seems to propagate downward. Hereinafter, we address the "top" and "bottom" parts of the streak image as they appear and not as the true orientation of the shock during experiments. The distance between the array and the water–air interface was 4 mm. Here, let us note that an almost 1 mm-thick water–air interface boundary appears because of a $\sim$9 mRad tilt between the water surface and the laser beam propagation direction. One can see an inclination of the shock trajectory in water when the strong shock, having a velocity of $\sim$2300 m/s, overlaps the weak shock[19] generated by the phase transition of wires earlier in the wire explosion stage. The velocity of the shock in air was found to be 1230 m/s.

A similar shadow streak image, with larger magnification (1:5), was obtained for the 27 kV charging voltage. This streak image showed that the shock in water propagates with a velocity of $\sim$2100 m/s. In this experiment, we obtained, together with the visible shadow of the shock in air propagating at $\sim$890 m/s, the shadow image of water flow having a rather smooth front in air, propagating with a velocity of $\sim$730 m/s. An additional experiment was conducted with a 2 mm-thick Perspex plate fixed at a 4 mm distance from the array [see Fig. 4(b)]. The purpose of this

experiment was to obtain the shock velocity in the Perspex plate. This will be used in an attempt to increase the water pressure prior to the fracturing of the plate. The velocities of the shock in water below the plate, inside the plate, and in the water above the plate were found to be 2100 m/s, 2800 m/s, and 1900 m/s, respectively.

Next, experiments with an Al target (12 mm in diameter and weighing 0.4 g) placed on top of different Perspex plates, varying in thickness and fixed at a 4 mm distance from the array, were performed. The purpose of these experiments was to determine whether the application of a fixed Perspex plate in front of the target can lead to an accumulation of water pressure, which, in turn, as the barrier "opens" (i.e., the plate fractures), produces larger values of the shock velocity in the target. These shots were performed with the generator charged to 27 kV, yielding a discharge current amplitude of 240 kA, peak power of 11 GW, and total energy deposited into the array of 3.5 kJ. A shadow streak image of the shock in water and the target trajectory in air with a 0.2 mm-thick Perspex plate are shown in Fig. 5(a). Here, one can see a strong shock propagating in water with a velocity of $\sim$2100 m/s and a strong shock propagating in air with a velocity of $\sim$600 m/s. Moreover, one can see two weak shocks, preceding the strong shock in air, with a velocity of $\sim$420 m/s, together with a small bump on the surface of the target, which appears almost simultaneously with the onset of a strong shock in air.

In Fig. 5(b), we present the PDV time-resolved measurements of Al targets (see Fig. 1, target 1) obtained in shots where Perspex plates with different thicknesses were placed between the target and the array at a distance of 4 mm from the array. The target dynamics exhibit fast ($\sim 1.4 \times 10^{-7}$ s) rising velocity, reaching a peak (described as the first peak velocity), which is accompanied by an approximately twofold sharp drop ($\sim 10^{-7}$ s) in the target velocity. The latter is followed by a $\sim$1 $\mu$s rise to $\sim$200 m/s. The typical time of the next gradual increase, to its maximal value, is $\sim$10 $\mu$s. This maximal value is defined as the saturated velocity. The main parameters of the target velocity obtained in these shots are listed in Table I. One can see that the application of the Perspex plate
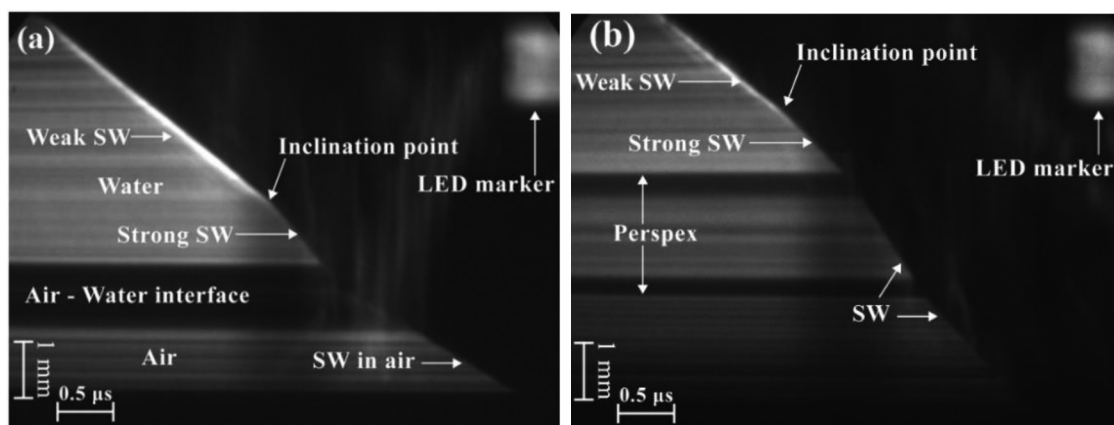


**FIG. 4.** Streak shadow images: (a) the shock and water flow without a target. The distance between the array and the water–air interface is 4 mm. The generator charging voltage is 35 kV. (b) Streak shadow image of the shock in water and Perspex plate of 2 mm thickness. The distance between the array and the plate is 4 mm. The generator charging voltage is 27 kV.
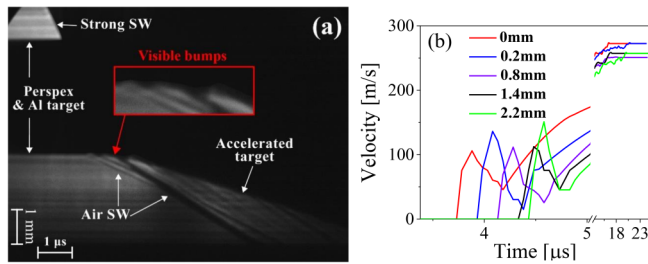
**FIG. 5.** (a) Shadow streak image of shocks in water and air together with Al target propagation in air when a 0.2 mm-thick Perspex plate is located at a 4 mm distance from the array. (b) Photonic Doppler velocimetry time-resolved velocity of the Al targets obtained in shots when Perspex plates with different thicknesses were located in front of the target at a distance of 4 mm from the array. The generator charging voltage is 27 kV, $t = 0$ of the streak image, and the velocity history is related to that of the discharge current.

leads to an increase in the value of the first peak velocity as compared to the case without this plate. However, the first peak and saturated values of the target velocity along with the rise time of the first peak velocity did not show dependence on the plate thickness within error of measurements and statistics of only two shots for each thickness of the Perspex plate. The first peak velocity maximal value of 150 m/s was obtained in the case of the thickest plate, with a thickness of 2.2 mm. In addition, the time delay between the strong shock entering the Perspex plate and the strong shock onset in the air increases significantly with the increase in the plate thickness, which relates to the increased time of flight of the shock propagation in the Perspex plate.

The interaction of the strong shock in water with the Perspex plate leads to its partial reflection toward the array while part of the shock propagates toward the target, where it experiences another reflection accompanied by the generation of a shock in the target. When the latter shock reaches the target's upper surface [bottom

**TABLE I.** Velocity and time delay parameters of the Al target located on top of Perspex plates of various thicknesses, which were positioned at a distance of 4 mm from the array. The generator charging voltage is 27 kV.

| Perspex thickness (mm) | First peak velocity (m/s)[a] | Rise time of first peak velocity (ns)[b] | Saturated velocity (m/s) | Time delay between shocks in water and air (ns)[c] |
|---|---|---|---|---|
| 0 | 90 | 130 | 285 | 580 |
| 0.2 | 132 | 140 | 270 | 650 |
| 0.8 | 110 | 120 | 250 | 865 |
| 1.4 | 130 | 110 | 265 | 1085 |
| 2.2 | 150 | 130 | 260 | 1385 |

[a]Error in measurements of the velocity was ±25 m/s.
[b]Error in measurements of the rise time of the first peak velocity was ±15 ns.
[c]Error in measurements of the time delay between shocks in water and air was ±40 ns.

part in Fig 5(a)], it generates the first weak shock in the air. The appearance of the second weak shock in the air is probably due to the strong shock reflections between the water–plate-target boundaries.

The results of these experiments showed that, as compared to the case where the plate is absent, the target's final velocity does not change within an error bar of the measurement. However, the measured values of the first peak target velocities measured with a Perspex plate are larger than without this plate. The latter can be related to the increase in the pressure at the vicinity of the plate, before it fractures. Lack of dependence in the velocity of the first peak vs the plate thickness can be related to relatively large (few tens of ns) time jitter in fracturing of these plates. The sudden realization of the pressure, which accompanies the plate fracture, leads to the generation of a strong shock in the target with a corresponding flow of material behind the shock front. Rarefaction of this shock at the target surface leads to the doubling of the material flow velocity at that location and the appearance of a bump responsible for the first spike in the target velocity. The latter is accompanied by the generation of a strong shock in the air propagating with a velocity of 600 m/s. The obtained "bump" can be related to the Hugoniot elastic limit (HEL), an initial phase of the "spall" phenomenon.[20] That is, the energy of the material behind the shock when the latter arrives at the surface of the target and is reflected is realized in a thin layer, leading to the appearance of a spall. In our experiments, visible spalls were not generated because the intensity of the shock was insufficient.

Based on the experimental results described above, next we performed shots (the generator was also charged to 27 kV) with the Al target located on top of a 0.6 mm-thick Perspex plate, which was positioned at different distances from the array. The experimental data showed that a decrease in the distance from 4 mm to 0.6 mm leads to an increase in the target first peak velocity to ∼200 m/s with a rise time of ∼100 ns and an increase in the target saturated velocity to ∼400 m/s within ∼20 $\mu$s [see Fig. 6(a)]. The kinetic energy of the target, associated with the measured saturated velocity, is ∼32 J. We also tested the target acceleration with a 1.2 mm-thick Perspex plate located 0.6 mm from the array. These shots showed a lower saturated velocity of the target, 330 m/s, but with a first peak velocity of 220 m/s.

To obtain scaling of the target velocity vs the energy stored in the capacitor banks, shots with an increased charging voltage of 35 kV were executed with the aforementioned Al target and 0.6 mm-thick Perspex plate located between the target and the array at a distance of 0.6 mm from the array. These experiments showed a first velocity peak of ∼ 325 m/s and a saturated velocity of the target ∼ 560 m/s, which results in a target kinetic energy of ∼63 J [see Fig. 6(b)]. The total energy deposited into the wire array was 5.8 kJ, which is ∼1.7 times larger than the energy deposition in the case where the charging voltage of the generator was 27 kV. However, the kinetic energy of the target was ∼2 times larger than in the case where the charging voltage was 27 kV.

To obtain scaling on the weight of the target, we conducted additional experiments with Al targets, having a diameter of 12 mm and a thickness of 0.5 mm and 0.02 mm, located on top of a 0.6 mm-thick Perspex plate positioned at a distance of 0.6 mm from the array (see Fig. 1, target 2). The results of these shots are
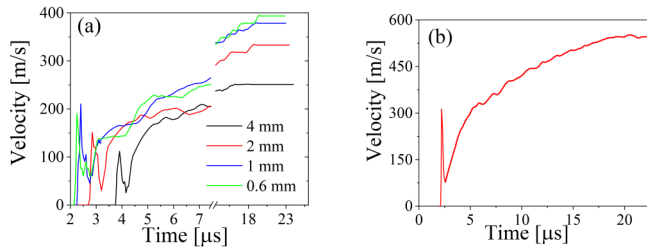
**FIG. 6.** Time-resolved velocity of Al targets obtained (a) with 0.6 mm-thick Perspex plates located between the target and the array at different distances from the array. The generator charging voltage is 27 kV; (b) with 0.6 mm-thick Perspex plates located between the target and the array at a distance of 0.6 mm from the array. The generator charging voltage is 35 kV; $t = 0$ is related to that of the discharge current.

shown in Fig. 7. One can see that in the case where its thickness was 0.5 mm, the saturated velocity acquired by the target reached 800 m/s and in the case where the target was thin (0.02 mm), the velocity peaked at $\sim$ 1360 m/s. A short time scale ($\sim$13.5 $\mu s$) is shown in Fig. 7(a) because of the fast decrease in the PDV signal intensity, probably related to an inclination of the target during its acceleration in these shots.

## IV. DISCUSSION

First, let us estimate the efficiency of target acceleration, $\eta$, which we define as the ratio between the target's acquired kinetic energy and the electrical energy deposited into the array. This estimation considers the Perspex plate weight of $m_{px} \sim 0.07$ g. During experiments, a 0.4 g target (see Fig. 1, target 1) with a 0.6 mm Perspex plate, located at 0.6 mm from the array, was used. Deposited energies of 3.5 kJ (charging voltage of 27 kV) and 5.8 kJ (charging voltage of 35 kV) resulted in target velocities of $\sim$ 400 m/s and $\sim$560 m/s, which correspond to a target kinetic energy of $\sim$38 J and $\sim$74 J, respectively. Considering that the target cross section was only $\sim$1/16 of the total area where the shock and water flow were generated, one can estimate that the value of $\eta$ is in the range of 17%–20%. In the case of a 0.5 mm-thick target with a
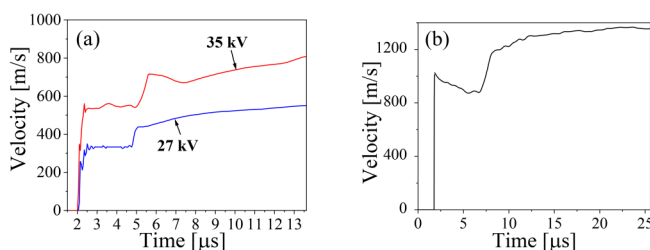


**FIG. 7.** Time-resolved velocities of 12 mm in diameter Al targets. (a) Target thickness of 0.5 mm and generator charging voltages of 27 kV and 35 kV. (b) Target thickness of 0.02 mm and generator charging voltage of 35 kV. The targets were located on top of a Perspex plate positioned at a distance of 0.6 mm from the array; $t = 0$ is related to that of the discharge current.

mass of 0.15 g (see Fig. 1, target 2), the kinetic energy reaches $\sim$50 J, corresponding to $\sim$14%, which is still more than the efficiency of methods based on target acceleration using magnetic field gradients.[21] Here, let us note that our estimates showed that one can neglect drag forces in the air, which exert negligible pressure on the target ($\leq 10^6$ Pa), as well as the magnetic pressure $B^2/2\mu_0$, which arises from currents induced in the target. Magnetic pressure was estimated to be rather small ($\leq 10^7$ Pa), meaning that it can be neglected during the process of target acceleration. Nevertheless, for future experiments, we are planning a design where the magnetic pressure will contribute to the target acceleration, in addition to the shock and generated water flow.

Now, let us discuss the evolution of target velocity, which is characterized by non-monotonic behavior, namely, a sharp rise in the velocity (first peak), which is followed by a decrease and later by a gradual increase to its saturated velocity. The first peak velocity can be considered as manifesting the HEL of the material and the spall phenomenon.[22,23]

Let us first consider the experiments without a target, performed at a 27 kV charging voltage of the generator and a 4 mm-thick water layer above the array. The streak image shows the shock in water propagating with velocity $D_1 = 2100$ m/s and water flow velocity in the air propagating with the velocity $U = 730$ m/s. The water flow velocity $U_1$ behind the shock front in water can be calculated using Rankine–Hugoniot relations[24] as $U_1 = D_1(\delta_1 - 1)/\delta_1$, where $\delta_1 = \rho_1/\rho_0$ is water compression, $\rho_0$ and $\rho_1$ are the undisturbed density of water and the density of water behind the shock front, respectively. The pressure behind the shock front can be calculated as $P_1 = \rho_0 U_1^2 \delta_1/(\delta_1 - 1)$. These relations, together with the polytropic EOS for water[25] in the Tait form $P - P_0 = \frac{\rho_0 c_0^2}{n}(\delta^n - 1) \approx 3 \times 10^8(\delta^{7.15} - 1)$, allows one to calculate water compression using the known shock velocity as $D_1 = \left[\frac{3 \times 10^8(\delta_1^{7.15} - 1)\delta_1}{[\rho_0(\delta_1 - 1)]}\right]^{1/2}$. Here, $n = 7.15$ is the adiabatic coefficient. Given the shock velocity of $D_1 = 2100$ m/s, the water compression ratio is $\delta_1 \approx 1.19$, the water flow velocity is $U_1 \approx 320$ m/s, and the pressure is $P_1 = 6.810^8$ Pa. At the water–air interface, because of the reloading and appearance of a reflected shock,[24] one can obtain a water flow velocity of $2 \times U_1 = 640$ m/s, which agrees satisfactorily with the experimental data. The velocity of the strong shock in air, visible in Fig. 5(a), was estimated to be $\sim$ 600 m/s, resulting in a flow velocity of compressed air behind the shock of 335 m/s and a compression ratio of $\delta_{air} \approx 2.27$.

Now let us consider experiments involving the acceleration of the Al targets. For the known velocity $D_1$ of the first shock interacting with the target in water, one can calculate the density and pressure behind its front, similar to the case described above. Here, we neglect by the attenuation of the shock in a thin Perspex plate, following the almost constant slope of the visible shock in Perspex, seen in Fig. 4(b). The interaction of the first shock with the target leads to the appearance of a shock reflected from the target and propagating with velocity $D_2$ toward the array. The second shock velocity $D_2$, water flow velocity $U_2$, compression $\delta_2 = \rho_2/\rho_0$, and pressure $P_2$ behind the shock front can be determined using mass and momentum conservation laws in the coordinate system related to this second shock. Here, let us note that in the mentioned

coordinate system, the direction of velocity $D_2$ is opposite to that of velocity $U_1$, but the directions of velocities $U_2$ and $U_1$ are the same. The values of $P_2$ and $\delta_2$ behind the front of the second shock relate to each other via the polytropic EOS. Following analyses, presented in detail in Ref. 26, one can write

$$U_2 + D_2 = \sqrt{\frac{(P_2 - P_1)\delta_1}{\rho_0 \delta_2 (\delta_2 - \delta_1)}},$$
$$U_1 - U_2 = \sqrt{\frac{(P_2 - P_1)(\delta_2 - \delta_1)}{\rho_0 \delta_2 \delta_1}}. \tag{1}$$

The interaction of the first shock with the target also leads to the appearance of a shock propagating in the target with velocity $D_t$, target compression ratio $\delta_t = \rho_t/\rho_{0t}$, and material flow velocity $U_t$ behind the shock front. Here, $\rho_t$ and $\rho_{ot}$ are the compressed and normal density of the target, respectively. As in the case of the first shock propagation in water, one can write

$$D_t = \sqrt{\frac{(P_t - P_{0t})\delta_t}{\rho_{0t}(\delta_t - 1)}},$$
$$U_t = \sqrt{\frac{(P_t - P_{0t})(\delta_t - 1)}{\rho_{0t}}}. \tag{2}$$

Here, $P_{0t}$ is the undisturbed pressure of the target. Now using the polytropic EOS for Al,[24] $P_t \approx 2.03 \times 10^{10}(\delta_t^4 - 1)$ and boundary conditions at the water–target interface, which dictate $U_2 = U_t$ and $P_2 = P_t$, one can solve Eqs. (1) and (2) extracting the values of $\rho_2, \rho_t, D_t, U_2 = U_t,$ and $P_2 = P_t$ for a given value of $D_1$, which also determines the values for $\rho_1$ and $U_1$.

In Fig. 8, we present the dependence of the pressure and density buildup vs the velocity of the first shock at the water–target interface in the case of an unmovable target, i.e., $U_2 = U_t = 0$. One can see a significant accumulation of the density and, consequently, the pressure at the interface boundary. This effect can be utilized
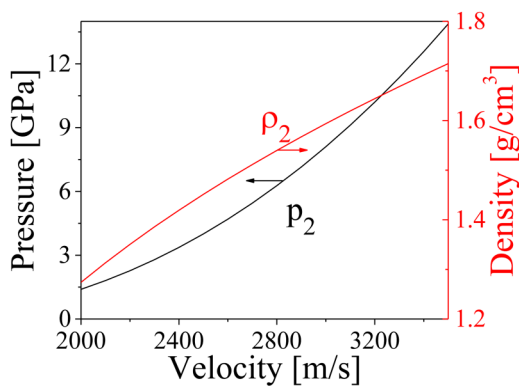
for increasing the target velocity and acceleration because of a significantly increased pressure gradient behind the target.

In Fig. 9, we present the dependences of the water and Al target densities $\rho_2$ and $\rho_t$, shock and material velocities ($U_t \neq 0$), and pressure in the target vs the first shock velocity in water. The case when the first shock velocity reaches ~3500 m/s corresponds to a pressure behind the shock front of ~$3.7 \times 10^9$ Pa. For this case, the material behind the shock front in the Al target acquires a velocity of ~1050 m/s with pressure inside the target reaching ~$8 \times 10^9$ Pa.

To estimate the pressure buildup in the array–plate gap, at the vicinity of the Perspex plate, additional modified numerical simulations were conducted. In these simulations, we chose several cells (let us call them "frozen" cells), corresponding to the water–Perspex boundary, where the computation of the thermodynamic parameters was artificially stopped. That is, at the time instant when the shock front arrived at the interface of "frozen" cells, we artificially turned off the EOS usage, thus keeping the water in the undisturbed state. This allows the water flow at that interface to cumulate pressure, while the shock bounces back toward the exploding array. The results of these numerical simulations showed that the increase in pressure depends strongly on the duration of the time interval during, which the EOS was turned off, i.e., the duration of the cells "freezing." For instance, without a "frozen" cell, the pressure behind the shock front was calculated to be ~$4.5 \times 10^8$ Pa and with "frozen cells," for ~60 ns, the pressure increases up to $16 \times 10^9$ Pa.

A straightforward comparison of the results of analytical and numerical modeling with the experimental results is rather challenging. Indeed, in our experiments, we used an Al target with a non-uniform cross-sectional area along its height (except targets of 0.5 mm and 0.02 mm thickness), and in a major part of the experiments, a Perspex plate was located between the array and the target. The shock generated by the array explosion interacts with the plate and later with the target, leading to the formation of a shock inside the target and a rarefaction shock. The latter propagates toward the array, is reflected from the expanding wires toward the target, and once more interacts with the target. This process of shock multi-reflections from the target and the array was considered in Ref. 12, where, using one-dimensional (1D) hydrodynamic (HD) simulations coupled with the EOS of water and the target



**FIG. 8.** Calculated dependences of the water density and pressure at the water–target interface vs the first shock velocity in the case of an unmovable target.
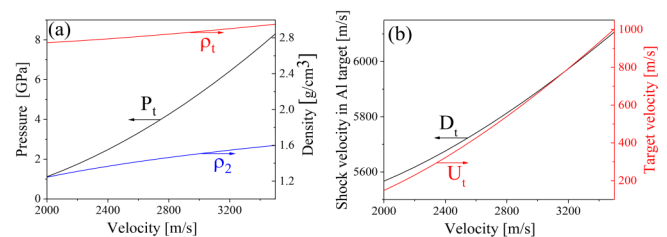


**FIG. 9.** Calculated dependences of (a) water and Al target densities ($\rho_2$ and $\rho_t$) together with pressure ($P_t$) inside the target vs first shock velocity in water; (b) shock and material velocities ($D_t$ and $U_t$) inside the target vs first shock velocity in water.

material, it was shown that this process might lead to a quasi-isentropic target compression. The critical compression ratio for Al, which falls under the criterion for quasi-isentropic compression (see Ref. 12), was estimated to be $\delta_{cr} \approx 1.12$, corresponding to a critical pressure and density $P_c = 1.16 \times 10^{10}$ Pa and $\rho_c \approx 3 \times 10^3$ kg/m$^3$, respectively. In the present experiment without Perspex plate in front of the target, according to the Rankine–Hugoniot relations, given the measured shock wave (SW) SW velocity in water ($D_1$), the target reached a compression ratio of $\delta_t \approx 1.02$, which holds to the mentioned quasi-isentropic criteria. However, in Ref. 12, the radial expansion of the exploded wires was not considered, although it leads to a decrease in the gap between the array and the target. The latter should lead to an additional compression of water and, in turn, increase in pressure, which becomes more pronounced with the decrease in the initial gap. Furthermore, a Perspex plate located in front of the target increases the water pressure prior to its fracture. However, the time delay of the plate fracture is not known and additional research is required to determine its value. Moreover, the density and pressure behind the front of the shock propagating in the plate, even with its velocity measured, cannot be calculated unless the EOS for Perspex is known. In addition, a decay of the shock in a 3 mm-thick target should be accounted for to compare the experimental with the simulation results. Moreover, perhaps the most important effect would be the dimensionality of the simulation. That is, the two-dimensional effect at the water–Perspex boundary might lead to the pressure re-loading because of water flow parallel to the Perspex surface, and thus, the 1DHD results may be interpreted as overestimated.

Here, let us note that in the case of a Perspex plate placed in front of the target, one can consider that the process of the target acceleration consists of several phases, namely, acceleration of the target due to the shock generated by the array explosion. This shock experiences partial reflection from the Perspex and target and penetrates into the target, leading to appearance of the material velocity behind its front. Also, with some time delay, the target is accelerated by the pressure gradient of compressed water when the Perspex plate fracturing occurs. Additional slow acceleration of the target occurs by the water flow generated by continuing radial expansion of the wires and the shock multi-reflections between the target and the array.

Thus, we compare only the results of experiments with the 0.02 mm-thick Al target located on top of the 0.6 mm Perspex plate. The plate was located at 0.6 mm from the array [see Fig. 7(b)]; i.e., the target was at an effective distance of 1.2 mm from the array. In these experiments, the target acquired a velocity of ~970 m/s within ~50 ns, and further, in the ms-timescale, it reached a saturated velocity of ~1360 m/s. Let us neglect the mass of the target ($m_{Al} \sim 55$ mg) and the attenuation of the shock during its propagation in the Perspex plate.[27] The 1DHD simulations described in Refs. 12 and 19 showed that, at a distance of 1.2 mm from the array, the shock velocity in water could be ~2200 m/s when the energy deposited into the array is ~6 kJ. In this case, the water flow velocity, water compression, and pressure behind the shock front will be ~ 370 m/s, 1.2, and ~$8 \times 10^8$ Pa, respectively. The interaction of this shock with the target should result in the velocity of the material at the target rear boundary layer being ~740 m/s, which is

significantly smaller than $V_{Al} = 970$ m/s of the first peak velocity that was obtained in the experiment. This apparent contradiction can be explained by pressure buildup behind the Perspex plate prior to its fracture. An estimation showed that this pressure buildup due to increased water density with compression up to 1.46 should be ~$4.2 \times 10^9$ Pa. A further, gradual increase in the target velocity up to ~ 1360 m/s can be explained by the target acceleration related to the continuous water flow, the velocity of which is governed by the array expansion and shock multi-reflections.

In the case of the 3 mm-thick target located on top of a Perspex plate, we associate the first peak in the target velocity, having ns-rise and fall timescales, with the initial phase of spall formation when the energy density realized in the boundary layer, due to the refraction wave, is not yet sufficient for complete spall formation. The decrease in this peak velocity is followed by a gradual velocity increase, acquired because of the continuous acceleration caused by the water flow behind the target.

In this research, we did not aim to measure Hugoniot, which requires systematic studies with variable incident shock intensities. The latter can be achieved in this approach either by changing the energy deposited into the wire array keeping a fixed distance between the target and the array or by varying this distance, given a fixed value of energy deposited into the array. The PDV data give the mass flow velocity $V_{Al}$ and the shadow streak images of the incident shock in water below the target and the shock in air above the target, with known thickness, gives the shock velocity $D_{Al}$ in the target. These data will allow one to obtain different values of pressure in the target as $P = \rho_0 D_{Al} V_{Al}$ and compressed Al material density as $\rho_{Al} = \rho_0 D_{Al}/(D_{Al} - V_{Al})$. Nevertheless, in experiments with the Perspex plate of 0.6 mm thickness, a maximal pressure of almost $9 \times 10^9$ Pa and compression of $\delta_t \approx 1.1$ was calculated based on the obtained shock velocity of 5900 m/s in the 0.5 mm-thick Al target and Al mass flow velocity of 550 m/s for the case of 35 kV charging voltage of the pulse generator.

## V. SUMMARY

The results of our experimental research showed that the acceleration of the target using the shock and water flow generated by an underwater electrical explosion of a wire array can be considered to constitute an efficient (up to 20%) approach. Using a moderate pulse generator with stored energy of ~6.5 kJ, streak shadow imaging, and PDV diagnostics, target velocities up to 1360 m/s were obtained. It was shown, both experimentally and by analytical modeling and numerical simulations, that this method, when a temporally unmovable barrier is applied, allows one to increase the pressure behind the target considerably. Another advantage of this approach is related to the additional water compression caused by the expanding wire array. In our next studies, we are planning to use a more powerful pulse generator that will deliver to the array current pulses with amplitude of ~500 kA within ~400 ns, as well as implementing other target designs to increase the target velocity by taking advantage of the magnetic pushing effect. Furthermore, we are planning to conduct numerical simulations that will account for the effects of wire expansion and shock multi-reflections.

## DATA AVAILABILITY

The data that support the findings of this study are available from the corresponding author upon reasonable request.

## REFERENCES

[1]B. A. Remington, R. M. Cavallo, M. J. Edwards, D. D.-M. Ho, B. F. Lasinski, K. T. Lorenz, H. E. Lorenzana, J. M. Mcnaney, S. M. Pollaine, and R. F. Smith, Astrophys. Space Sci. **298**, 235–240 (2005).

[2]T. Sasaki, T. Takahashi, T. Ohuchi, Y. Kawaguchi, K. Takahashi, T. Kikuchi, T. Aso, N. Harada, K. Horioka, H. Nagatomo, and S. Fujioka, Energy Procedia **71**, 261–267 (2015).

[3]V. E. Fortov and I. T. Iakubov, *The Physics of Non-Ideal Plasma* (World Scientific, Singapore, 2000).

[4]A. M. Evans, N. J. Freeman, P. Graham, C. J. Horsfield, S. D. Rothman, B. R. Thomas, and A. J. Tyrrell, "Hugoniot EOS measurements at Mbar pressures," Laser Part. Beams **14**(2), 113–123 (1996).

[5]L. C. Chhabildas, L. M. Barker, J. R. Asay, T. G. Trucano, G. I. Kerley, and J. E. Dunn, "Launch capabilities to over 10 km/s," in *Shock Compression of Condensed Matter—1991* (Elsevier, 1992), pp. 1025–1031.

[6]D. B. Sinars, M. A. Sweeney, C. S. Alexander *et al.*, Phys. Plasmas **27**, 070501 (2020).

[7]R. W. Lemke, M. D. Knudson, D. E. Bliss, K. Cochrane, J.-P. Davis, A. A. Giunta, H. C. Harjes, and S. A. Slutz, J. Appl. Phys. **98**, 073530 (2005).

[8]A. Grinenko, S. Efimov, A. Fedotov, I. Schnitzer, and Y. E. Krasik, J. Appl. Phys. **100**, 113509 (2006).

[9]S. Efimov, V. T. Gurovich, G. Bazalitski, A. Fedotov, and Y. E. Krasik, J. Appl. Phys. **106**, 073308 (2009).

[10]A. Rososhek, S. Efimov, A. Goldman, S. V. Tewari, and Y. E. Krasik, Phys. Plasmas **26**, 053510 (2019).

[11]A. Rososhek, S. Efimov, A. Virozub, D. Maler, and Y. E. Krasik, Appl. Phys. Lett. **115**, 074101 (2019).

[12]V. Gurovich, A. Virozub, A. Rososhek, S. Bland, R. B. Spielman, and Y. E. Krasik, J. Appl. Phys. **123**, 185902 (2018).

[13]G. Bazalitski, V. Ts. Gurovich, A. Fedotov-Gefen, S. Efimov, and Ya. E. Krasik, Shock Waves **21**, 321–329 (2011).

[14]*SESAME: The Los Alamos National Laboratory Equation-of-State Database*, edited by S. P. Lyon and J. D. Johnson, Los Alamos National Laboratory Report No. LA-UR-92-3407, 1992.

[15]S. Efimov, A. Fedotov, S. Gleizer, V. T. Gurovich, G. Bazalitski, and Y. E. Krasik, Phys. Plasma **15**, 112703 (2008).

[16]B. M. Kovalchuk, A. V. Kharlov, V. B. Zorin, and A. A. Zherlitsyn, Rev. Sci. Instrum. **80**, 083504 (2009).

[17]D. H. Dolan, Rev. Sci. Instrum. **81**, 053905 (2010).

[18]D. H. Dolan and T. Ao, "SIRHEN: A data reduction program for photonic Doppler velocimetry measurements," Sandia Report No. SAND2010-3628, June 2010.

[19]A. Rososhek, S. Efimov, S. V. Tewari, D. Yanuka, and Y. E. Krasik, Phys. Plasmas **25**, 102709 (2018).

[20]D. Grady, *Physics of Shock and Impact, Volume 1; Fundamentals and Dynamic Failure* (IOP Publishing, Bristol, 2017).

[21]T. Ao, J. R. Asay, S. Chantrenne, M. R. Baer, and C. A. Hall, Rev. Sci. Instrum. **79**, 013903 (2008).

[22]S. V. Razorenov, G. I. Kanel, K. Baumung, and H. J. Bluhm, "Hugoniot elastic limit and spall strength of aluminum and copper single crystals over a wide range of strain rates and temperatures," AIP Conf. Proc. **620**, 503 (2002).

[23]R. F. Trunin, *Shock Compression of Condensed Materials* (Cambridge Univ. Press., 2005).

[24]Y. B. Zeldovich and Y. P. Raizer, *Physics of Shock Waves and High-Temperature Hydrodynamic Phenomena*, 2nd ed. (Academic, New York, 1967).

[25]R. H. Cole, *Underwater Explosion* (Princeton University Press, Princeton, NJ, 1948).

[26]O. Antonov, S. Efimov, V. T. Gurovich, D. Yanuka, D. Shafer, and Y. E. Krasik, J. Appl. Phys. **115**, 223303 (2014).

[27]R. Khurana, P. C. Gautam, R. Rai, A. Kumar, A. C. Sharma, and M. Singh, J. Phys. Conf. Ser. **377**, 012051 (2012).